Resolution, stability and efficiency of resistivity tomography estimated from a generalized inverse approach

Originally published in:
Geophysical Journal International 153(2), https://doi.org/10.1046/j.1365-246X.2003.01890.x

Geophys. J. Int. (2003) **153,** 305–316

Resolution, stability and efficiency of resistivity tomography estimated from a generalized inverse approach

Sven Friedel[1,2]

[1] *Institute for geotechnical engineering, ETH Hoenggerberg,* 8093 *Zurich, Switzerland*
[2] *Institut für Geophysik und Geologie, Universität Leipzig, Talstraße* 35, 04103 *Leipzig, Germany. E-mail: friedel@rz.uni-leipzig.de*

Accepted 2002 September 3. Received 2002 July 22; in original form 2002 April 15

SUMMARY

Inconsistencies between an object and its image delivered by tomographical methods are inevitable. Loss of information occurs during the survey through incomplete and inaccurate data sampling and may also be introduced during the inverse procedure by smoothness constraints inadequate to the resolving power of the experimental setup.

A quantitative appraisal of image quality (spatial resolution and image noise) is therefore not only required for successful interpretation of images but can be used together with measures of efficiency of the experimental design to optimize survey and inverse procedures.

This paper introduces a low-contrast inversion scheme for electrical resistivity tomography that supports the reconstructed image with estimates of model resolution, model covariance and data importance. The algorithm uses a truncated pseudo-inverse and a line search approach to determine the maximum number of degrees of freedom necessary to fit the data to a prescribed target misfit. Though computationally expensive, the virtue of the method is that it reduces subjectivity by avoiding any empirically motivated model smoothness constraints. The method can be incorporated into a full non-linear inversion scheme for which *a posteriori* quality estimates can be calculated.

In a numerical 2-D example the algorithm yielded reasonable agreement between object and image even for moderate resistivity contrasts of 10:100:1000. On the other hand, the resolving power of an exemplary four-electrode data set containing classical dipole–dipole and non-conventional configurations was shown to be severely affected by data inaccuracy.

Insight into the resolving power as a function of space and data accuracy can be used as a guideline to designing optimized data sets, smoothness constraints and model parametrization.

Key words: electrical resistivity tomography, inverse modelling, resolution, stability.

1 INTRODUCTION

Electrical resistivity tomography (ERT) in its geophysical application is a method that attempts to reconstruct an image of the resistivity inside the Earth from current and voltage measurements made on its surface or in boreholes.

The method comprises a measuring process and a reconstruction process both of which must be regarded as non-ideal, leading to a loss of information on the object during the imaging procedure.

Present-day instruments allow the acquisition of several thousand resistance readings and numerous algorithms have been invented that allow the inference of finely discretized model estimates usually presented as 2-D or 3-D images. However, a successful interpretation of images requires an assessment of their quality. Furthermore, quantification of the loss of information occurring during the imaging process would also allow the comparison of different imaging systems and provide means for improving their design.

Questions concerning the quality and efficiency of the imaging process are becoming increasingly important, although they have puzzled scientists and users since the early years of the method. Some of these questions refer to:

(1) resolution: how much does the image resemble the object?
(2) stability: what artefacts can be expected to arise from propagation of data error into image noise?
(3) efficiency: how can the design of measurement and inversion be optimized to achieve maximum information?

The aim of this study is to present a low-contrast inversion scheme that besides a model estimate also yields measures for resolution and noise of the image as well as information on the efficiency of the experimental design. The method uses a linearization of the forward problem and a generalized inverse constructed by truncated singular-value decomposition, reducing the subjectivity usually imposed by empirical smoothness constraints.

The paper is organized in the following way: first, approaches to quantifying imaging quality are reviewed, next the problem is formulated in a mathematical manner and model resolution, model covariance and data resolution as defined from inverse theory are

introduced to describe the consequences of non-uniqueness. The main part of the paper deals with the actual construction of these functionals for the resistivity problem and the derivation of intuitively usable estimates as a radius of resolution, a binary flag of geometrical distortion and a percentage of image noise. The inversion scheme is tested on a synthetic 2-D model using classical and non-classical measurement configurations. Finally, the effect of accurate and inaccurate data on image resolution is discussed and the efficiency of the experimental design is assessed.

2 APPROACHES TO QUANTIFYING IMAGING QUALITY

Numerous approaches addressing the above questions have been presented by geophysicists and by the community of medical electrical impedance tomography. Most of them fall into one of the following categories.

Analytical sensitivity studies assessing the influence of a differential model parameter change on individual measurements were introduced by Evjen (1938) for 1-D layered models and have led to the definition of depth of investigation extensively discussed in the 1970s and concisely summarized by Barker (1989). Advanced analysis of sensitivity in 2-D (Barker 1979) and 3-D, including their deformation by inhomogeneities (Spitzer 1998), brought fundamental insight into the typical structure of apparent resistivity anomalies.

Numerical perturbation studies examine whether the anomalous response of predefined features in the ground exceed the limits of detectability (van Nostrand 1953; Dey *et al.* 1975; Apparao *et al.* 1992). Both of the above approaches suffer from the disadvantage that they only investigate the influence of a model perturbation on individual or sets of data, but not on the image itself.

Numerical model resolution studies based on the application of a reconstruction algorithm on synthetically calculated data contaminated with noise compare directly the similarity between the model and the image. The comparison of either a set of survey procedures, a set of inversion algorithms, a set of predefined models or a combination of such sets, is made visually (Sasaki 1992; Beard & Tripp 1995; Dahlin & Loke 1998; Dahlin & Bing 2001) or by definition of model-misfit functions (Olayinka & Yaramanci 2000).

Besides such exemplary studies and heuristic approaches it has always been a temptation to derive more general and analytical measures for the appraisal of imaging quality in impedance tomography.

Resolution analysis based on local sums of sensitivity for all measurements contained in a set were proposed especially for SIRT-like reconstruction schemes (Kemna 1995; Friedel 1997; Seichter 1998) but were also considered for conventional matrix inversion techniques (Park & Van 1991).

Oldenburg & Li (1999) present a method to measure the depth of investigation by quantifying how much each region of the image is constrained by the data and how much by subjective model constraints. The procedure considers the full non-linear problem and analyses the difference in two or more inversion results attained with different model constraints.

The idea of Backus & Gilbert (1968) to consider the imaging process as an averaging filter, the properties of which can be described and influenced, has been used in several approaches, but mainly for 1-D resistivity sounding problems, such as to construct averaging kernel functions (Oldenburg 1978), to derive upper and lower bounds for the model parameters (Oldenburg 1983), or to optimize the design of electromagnetic (EM) surveys (Maurer & Boerner 1998; Maurer *et al.* 2000). Only recently has image appraisal for 2-D and 3-D electromagnetic inversion been suggested Alumbaugh & Newman (2000). Unlike in this paper the authors have used classical smoothness constraints.

Considerable research has been devoted to analytical measures of resolution and stability in medical impedance tomography. This paper was most inspired by the approaches of Dobson & Santosa (1994) and Avis & Barber (1994) who analysed the condition numbers and singular-value spectra of various sets of electrode configurations.

In geoelectrical inversion the SVD approach has received relatively little attention and has so far been applied only to 1-D resistivity problems (Inman *et al.* 1973), presumably because of its high computational costs. The same applies partly to seismic tomography, where the forward problem is generally sparse and resolution has been exhaustively studied (e.g. Aki & Richards 1980; Nolet 1987; Iyer & Hirahara 1993), but only few attempts were made to compute SVD for realistic large problems (see references in Minkoff 1996).

However, though computationally expensive, the method seems promising for 2-D and 3-D resistivity problems, since it offers general insight into non-uniqueness, resolving power, stability and efficiency while introducing no, or only a few, subjective constraints.

3 METHOD

3.1 Causes and consequences of non-uniqueness

The mathematically reassuring facts that the inverse resistivity problem has a unique solution for 2-D and 3-D objects have been proven rigorously in significant papers by Kohn & Vogelius (1985) and Sylvester & Uhlmann (1987). However, the conditions for the unique reconstruction of the resistivity inside an object from current and voltage measurements made on its boundary are very demanding. Voltage and current must be known: (1) as continuous functions on the whole boundary, (2) for a complete set of spatial patterns of the driving current and (3) with infinite precision. A similar uniqueness theorem was already proven by Langer (1933) for the 1-D layered Earth.

Geophysical applications of ERT systems, however, cover only a limited part of the Earth, employ a finite number of electrodes and comprise measurements of limited precision. From this incompleteness of information arises the non-uniqueness encountered in all practical cases.

ERT comprises two fundamental operations, measurement and image reconstruction. By measuring the injected current and potential differences for a given set of electrode configurations the resistivity $m(\mathbf{r})$ of an object is mapped during the forward operation $\mathcal{F}$ on to a set of data

$$\mathbf{d} = \mathcal{F}m + \mathbf{n}, \tag{1}$$

usually apparent resistivities. It is assumed that data contains additive noise $\mathbf{n}$. Afterwards, the data are treated with a reconstruction scheme $\tilde{\mathcal{F}}^{-1}$, an approximation to the inverse of $\mathcal{F}$, to obtain a model estimate (image)

$$m^{\text{est}} = \tilde{\mathcal{F}}^{-1}\mathbf{d} = \tilde{\mathcal{F}}^{-1}\mathcal{F}\mathbf{m} + \tilde{\mathcal{F}}^{-1}\mathbf{n}, \tag{2}$$

which yields a prescribed target misfit between the measured data $\mathbf{d}$ and the predicted data

$$\mathbf{d}^{\text{pred}} = \mathcal{F}m^{\text{est}} = \mathcal{F}\tilde{\mathcal{F}}^{-1}\mathbf{d} \tag{3}$$

and may comply with additional constraints. Here it is assumed that the synthetic forward operator sufficiently approximates the physics

of the problem. From eq. (2) it can be seen that the similarity of image and object is ruled by $\tilde{\mathcal{F}}^{-1}\mathcal{F} := \mathcal{R}_M$, the model resolution operator. From eq. (3) it follows that the agreement between data and predicted data is described by $\mathcal{F}\tilde{\mathcal{F}}^{-1} := \mathbf{R}_D$, the data resolution matrix. For non-linear imaging systems both of these operators depend on the object itself. The second term in (2) describes the image noise. Since the true error is never known, usually the propagation of data covariance is considered. For problems that are not too non-linear the model covariance matrix

$$[\mathrm{cov}\,\mathbf{m}^{\mathrm{est}}] = \tilde{\mathcal{F}}^{-1}[\mathrm{cov}\,\mathbf{d}]\tilde{\mathcal{F}}^{-1T}. \tag{4}$$

can be used as an estimate of image noise (Menke 1989). Before approximations to the functionals $\mathcal{R}_M$, $\mathbf{R}_D$ and $[\mathrm{cov}\,\mathbf{m}^{\mathrm{est}}]$ are constructed for the resistivity problem a brief schematic example shall illustrate what information can be expected.

The model resolution operator describes the mapping from the object to the image for noise-free data. Accounting for non-linearity it can be expressed as a model-dependent averaging kernel

$$m^{\mathrm{est}}(\mathbf{r}) = \int_\Omega R_M(m, \mathbf{r}, \mathbf{r}')m(\mathbf{r}')\,d^3r'. \tag{5}$$

It describes what region of the model is projected into the image at point $\mathbf{r}$. Another way of thinking about the weighting kernel is to regard it as a point spread function (PSF), which describes what disturbance a delta-like model perturbation will cause in the image. Fig. 1 illustrates general properties that the resolution operator may have.

For an ideal imaging process, the resolving kernel would equal a delta function $R_M(m, \mathbf{r}, \mathbf{r}') = \delta(\mathbf{r} - \mathbf{r}')$ independently of the model and location. For continuous inverse problems with incomplete data this perfect resolution can never be attained, but the resolving kernel works as an averaging filter. Image cells will contain localized averages of the object properties and the width of the kernel is a measure of resolution. Furthermore, the resolving kernel describes geometrical distortions that may occur in the image if the maximum of the PSF lies off the diagonal or R_M contains significant side lobes.

A similar weighted averaging relation for the data space is interpreted as follows. If the data resolution matrix $\mathbf{R}_D$ is independent of the model and equal to the identity matrix, all data can be independently resolved, otherwise the predicted data are averages of the measured data, which indicates redundancy. Therefore, this matrix yields a measure of the efficiency of a forward procedure. Though the usefulness of the measures R_M, $\mathbf{R}_D$ and $[\mathrm{cov}\,\mathbf{m}^{\mathrm{est}}]$ is obvious, the actual construction for the inverse resistivity problem is complicated by the fact, that the forward problem is non-linear and the approximate inverse an iterative procedure. In the following, approximations will be introduced that allow the calculation of useful estimates to the functionals.

3.2 Construction and decomposition of the forward map

The forward operation for the resistivity problem is usually given implicitly by Poisson's equation. Alternatively, it can be expressed as a non-linear integral equation making use of the sensitivity function. For each measurement the latter is usually derived by a truncated Taylor expansion:

$$\mathcal{F}_i[m + \Delta m] = \mathcal{F}_i[m] + \int_\Omega \left.\frac{\partial \mathcal{F}_i}{\partial m}\right|_m \Delta m\,d^3r. \tag{6}$$

and relates model and data perturbations through the Fréchet derivative

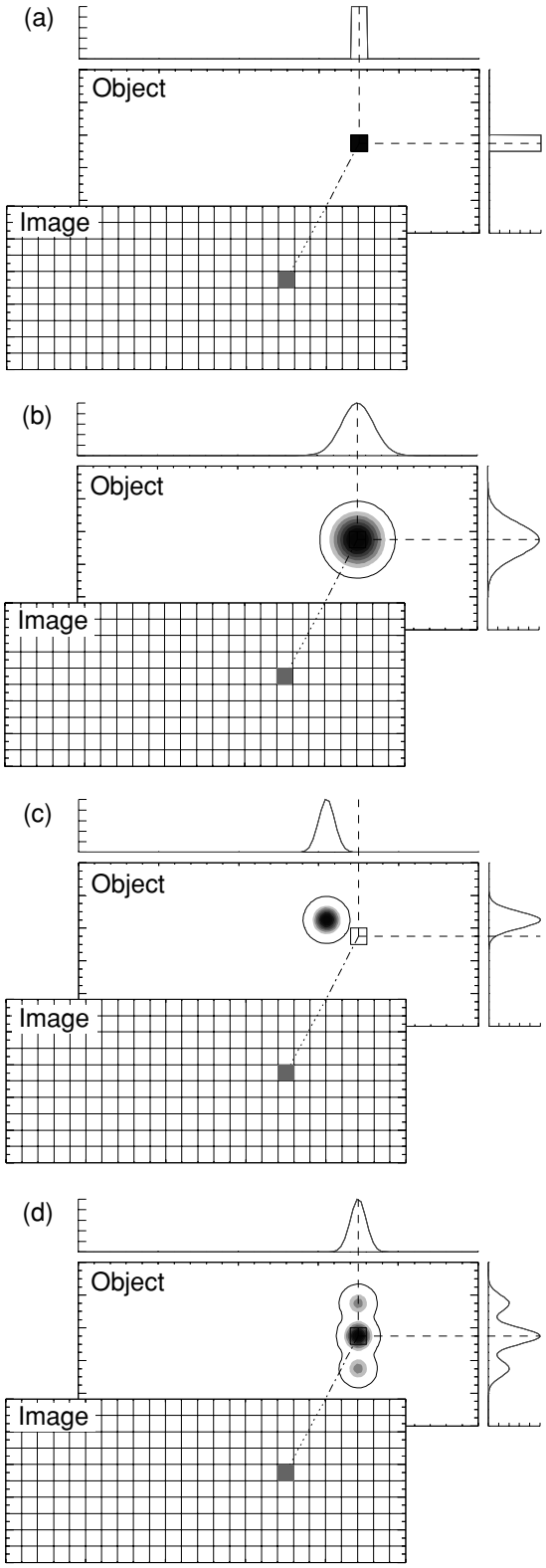

Figure 1. Schematic model resolution operator: (a) for a discrete model an imaging process can be regarded to be ideal in the area of a certain image cell, if its value equals the average of the respective object subdomain. In this case the model parameter was chosen perfect according to the resolving power of the data. (b) Contrast deficiency occurs if the support of the point spread function extends the limits of the respective cell. (c) Geometrical distortion occurs if the maximum of the PSF lies off the diagonal or (d) the weighting kernel has significant side lobes.

$$\Delta d_i = \int_\Omega S_i(m, \mathbf{r}) \Delta m \, d^3 r \text{ with } S_i(m, \mathbf{r}) = \left. \frac{\partial \mathcal{F}_i}{\partial m} \right|_m . \tag{7}$$

As a peculiarity of the dc resistivity problem, not generally valid for non-linear problems, the Fréchet derivative serves as an absolute weighting function in the non-linear integral formulation of the forward problem.

$$d_i = \mathcal{F}_i m = \int_\Omega S_i(m, \mathbf{r}) m(\mathbf{r}) \, d^3 r. \tag{8}$$

A proof of this relation was derived by Gómez-Treviño (1987) from the scaling properties of Maxwell's equation. We have recently presented another proof based only on the reciprocity theorem (Brunner *et al.* 1999). The equivalence of the Fréchet derivative and the absolute weighting function has far reaching implications: it allows an easy calculation of the forward response of an arbitrarily inhomogeneous model if only the sensitivity is known, since the linearized Taylor expansion no longer contains an absolute term. Furthermore, it follows for the homogeneous case, if resistivity and apparent resistivity are chosen as data and parameters such that $\int_\Omega S_i(m^{\text{hom}}, \mathbf{r}) \, d^3 r = 1$.

We now consider an arbitrary set of apparent resistivity data $\mathbf{d} = (d_1, \ldots, d_N)$ measured on a system of L electrodes. Data are assumed to be uncorrelated and scaled to uniform variance by a diagonal matrix $\mathbf{D}$ containing the reciprocal data standard deviations $D_{ii} = 1/\sigma_i$. For all discrete models linearly close to $\mathbf{m} = (m_1, \ldots, m_M)$ the linearized discrete and scaled forward operation can be approximated by

$$\mathbf{D}\mathcal{F}[m + \Delta m] := \mathbf{DS}(\mathbf{m} + \Delta \mathbf{m}). \tag{9}$$

Non-uniqueness of the inverse problem can be investigated by discriminating the kernel of the forward map from its null-space that contains indistinguishable models. This can be achieved by singular-value decomposition (Golub & van Loan 1989) of the matrix $\mathbf{DS}$ into

$$\mathbf{DS} = \mathbf{UWV}^{\mathrm{T}} = [\mathbf{U}_p, \mathbf{U}_0] \begin{bmatrix} \mathbf{W}_p & 0 \\ 0 & 0 \end{bmatrix} \begin{bmatrix} \mathbf{V}_p^{\mathrm{T}} \\ \mathbf{V}_0^{\mathrm{T}}, \end{bmatrix} \tag{10}$$

where $\mathbf{U} \in \mathrm{R}^{N \times N}$ and $\mathbf{V} \in \mathrm{R}^{M \times M}$ denote unitary matrices formed by complete sets of data and model eigenvectors, respectively. The matrix

$$\mathbf{W} = \text{diag}(w_1, \ldots, w_q), q = \min(M, N)$$

is diagonal and contains the singular values

$$w_1 \geq \cdots \geq w_p \geq w_{p+1} = \cdots = w_q = 0.$$

The rank p of $\mathbf{DS}$ denotes the number of theoretically linear independent data. Elementary circuit theory tells us that for an L-pole network the maximum number of independent resistance measurements is $p_{\max} = L(L-1)/2$. This means that however complicated a resistor network may be, or even if L-poles are connected to a continuous body not more than $p_{\max}$ characteristic transfer impedances or degrees of freedom can be reconstructed. A natural choice of degrees of freedom are the model eigenvectors. The model space $\mathcal{M}$ can be separated into two orthogonal subspaces

$$\mathcal{M} = \mathcal{M}_p \oplus \mathcal{M}_0 \quad \text{with}$$

$$\mathcal{M}_p := \{\mathbf{m} \in \mathcal{M} \mid \mathbf{DSm} \neq 0\} = \text{span}(\mathbf{V}_p) \tag{11}$$

$$\mathcal{M}_0 := \{\mathbf{m} \in \mathcal{M} \mid \mathbf{DSm} = 0\} = \text{span}(\mathbf{V}_0). \tag{12}$$

Model eigenvectors exhibit a natural ordering according to their distinguishability. This means that the rms data response of a model containing only a single eigenvector V_l is proportional to the respective eigenvalue w_l since the orthonormality of the eigenvectors leads to

$$\|\mathbf{DS} V_l\| = \left\|\mathbf{UWV}^{\mathrm{T}} V_l\right\| = \|U_l w_l\| = w_l.$$

In the presence of noise it is therefore very likely that model components corresponding to very small eigenvalues yield data well below the threshold of detectability. It is therefore justified to regard such model eigenvectors as lying effectively in the null-space. The method of the truncated pseudo-inverse (Shim & Cho 1981) achieves this by truncation of the singular-value spectrum to the first r values while zeroing the remainder $w_{r+1} = \cdots = w_p = 0$. The truncated pseudo-inverse is given by

$$(\mathbf{DS})^\dagger = \mathbf{V}_r \mathbf{W}_r^{-1} \mathbf{U}_r^{\mathrm{T}},$$

where r is the number of effectively non-vanishing singular values. The positive effect of truncation is a gain in stability since the propagation of data error into image noise is proportional to the reciprocal of the smallest singular value. On the other side truncation imposes a severe loss of information because of the exclusion of image components. A method to determine r carefully according to data quality is presented in the next section.

3.3 Approximate inverse and quality functionals

During the image reconstruction a model estimate is often found by minimizing the weighted residual functional

$$\chi^2(\mathbf{m}^{\text{est}}, \mathbf{d}) = \sum_{i=1}^{N} \left(\frac{d_i - \mathcal{F}_i[\mathbf{m}^{\text{est}}]}{\sigma_i} \right)^2 \tag{13}$$

$$= \|\mathbf{D}(\mathbf{d} - \mathcal{F}[\mathbf{m}^{\text{est}}])\|^2. \tag{14}$$

Since the data contain noise that should not be fitted some authors prefer to minimize not $\chi^2(\mathbf{m}^{\text{est}}, \mathbf{d})$ but its difference with respect to a target misfit

$$\left|\chi^2(\mathbf{m}^{\text{est}}, \mathbf{d}) - \chi_*^2\right| = \min! \tag{15}$$

Prescribing a target misfit χ_*^2 of unity results in residuals that on average equal the standard deviations of the data, a reasonably objective choice. Since the minimization problem (15) has no unique solution, most inversion schemes add a penalty functional that forces the image to be not unnecessarily complex. Most approaches use a smoothing matrix weighted with a smoothing parameter (both empirically defined) to make the inverse problem unique without sacrificing too much resolution. Even if an optimum smoothing parameter, which produces exactly the target misfit, is calculated during an Occam inversion (deGroot-Hedlin & Constable 1990; LaBrecque *et al.* 1996), subjectivity remains in the choice of the smoothness functional (the order of the derivative matrix, the increase of regularization with depth, etc.). Today most inversion schemes address this problem empirically, whereas ideally it should be addressed with respect to the resolving power of the measurement scheme. In this study the truncated SVD inversion is used because it introduces only little subjectivity. As a constraint to the minimization problem (15) it is required that the model estimate shall have no component in the effective null-space $\mathbf{V}_0^{\mathrm{T}} \mathbf{m}^{\text{est}} = 0$ that cannot be distinguished by measurements.

The minimization problem is attacked by assuming that a solution is found in step $n+1$ in which case the response can be expanded to

$$\mathcal{F}\left[\mathbf{m}_{n+1}^{\text{est}}\right] = \mathcal{F}\left[\mathbf{m}_{n}^{\text{est}}\right] + \mathbf{S}\left(\mathbf{m}_{n+1}^{\text{est}} - \mathbf{m}_{n}^{\text{est}}\right). \tag{16}$$

Inserting eq. (16) in eq. (15) an iterative formula can be found

$$\mathbf{m}_{n+1}^{\text{est}} = \mathbf{m}_{n}^{\text{est}} + (\mathbf{DS})^{\dagger}\mathbf{D}\left(\mathbf{d} - \mathcal{F}\left[\mathbf{m}_{n}^{\text{est}}\right]\right), \tag{17}$$

where $\mathbf{DS})^{\dagger}$ represents the truncated SVD pseudo-inverse. Assuming now that the model $\mathbf{m}_{n}^{\text{est}}$ is already linearly close to the true model $\mathbf{m}$, i.e.

$$\mathbf{d} = \mathcal{F}[\mathbf{m}] + \mathbf{n} = \mathcal{F}\left[\mathbf{m}_{n}^{\text{est}}\right] + \mathbf{S}\left(\mathbf{m} - \mathbf{m}_{n}^{\text{est}}\right) + \mathbf{n} \tag{18}$$

we obtain

$$\begin{aligned}\mathbf{m}_{n+1}^{\text{est}} &= \mathbf{m}_{n}^{\text{est}} + (\mathbf{DS})^{\dagger}\mathbf{DS}\left(\mathbf{m} - \mathbf{m}_{n}^{\text{est}}\right) + (\mathbf{DS})^{\dagger}\mathbf{Dn} \\ &= \mathbf{R}_{M}\mathbf{m} + (\mathbf{I} - \mathbf{R}_{M})\mathbf{m}_{n}^{\text{est}} + (\mathbf{DS})^{\dagger}\mathbf{Dn}.\end{aligned} \tag{19}$$

Here the model resolution operator is defined as

$$\mathbf{R}_{M} = (\mathbf{DS})^{\dagger}\mathbf{DS} = \mathbf{V}_{r}\mathbf{W}_{r}^{-1}\mathbf{U}_{r}^{\mathrm{T}}\mathbf{U}_{p}\mathbf{W}_{p}\mathbf{V}_{p}^{\mathrm{T}} = \mathbf{V}_{r}\mathbf{V}_{r}^{\mathrm{T}}.$$

The model estimate is obviously built up from three components: it resembles the object as far as $\mathbf{R}_{M}$ allows; where no resolution can be provided the previous model is filled in; and it contains a component of propagated noise. Considering unwanted null-space components it follows from $\mathbf{V}_{r} \perp \mathbf{V}_{0}$ that

$$\mathbf{V}_{0}^{\mathrm{T}}\mathbf{m}_{k+1}^{\text{est}} = \mathbf{V}_{0}^{\mathrm{T}}\mathbf{m}_{k}^{\text{est}}. \tag{20}$$

A model component in the null-space can obviously only be introduced by the starting model but does not result from noise.

An expression similar to (19) for the data resolution matrix can be found by applying the forward procedure to the model estimate (17)

$$\begin{aligned}\mathbf{d}_{n+1}^{\text{pred}} &= \mathcal{F}\left[m_{n+1}^{\text{est}}\right] = \mathcal{F}\left[m_{n}^{\text{est}}\right] + \mathbf{S}(\mathbf{DS})^{\dagger}\mathbf{D}\left(\mathbf{d} - \mathcal{F}\left[\mathbf{m}_{n}^{\text{est}}\right]\right) \\ &= \mathbf{d}_{n}^{\text{pred}} + \mathbf{DS}(\mathbf{DS})^{\dagger}\left(\mathbf{d} - \mathbf{d}_{n}^{\text{pred}}\right) \\ &= \mathbf{R}_{D}\mathbf{d} + (\mathbf{I} - \mathbf{R}_{D})\mathbf{d}_{n}^{\text{pred}} \text{ with}\end{aligned} \tag{21}$$

$$\mathbf{R}_{D} = \mathbf{DS}(\mathbf{DS})^{\dagger} = \mathbf{U}_{p}\mathbf{W}_{p}\mathbf{V}_{p}^{\mathrm{T}}\mathbf{V}_{r}\mathbf{W}_{r}^{-1}\mathbf{U}_{r}^{\mathrm{T}} = \mathbf{U}_{r}^{\mathrm{T}}\mathbf{U}_{r}. \tag{22}$$

Finally, an estimate for the model covariance is constructed by inserting the weighted forward procedure and its generalized inverse in eq. (4)

$$\left[\operatorname{cov}\mathbf{m}_{k+1}^{\text{est}}\right] = (\mathbf{DS})^{\dagger}[\operatorname{cov}\mathbf{d}](\mathbf{DS})^{\dagger\mathrm{T}}. \tag{23}$$

3.4 A single-step SVD inversion scheme

The linearized theory presented in the previous section can be applied to the full non-linear problem as an *a posteriori* appraisal of resolution, stability and information density if the sensitivity matrix of the final inversion step is used. In the following numerical example a single-step inversion algorithm is presented that uses the homogeneous background as a starting model $\mathbf{m}_{0}^{\text{est}}$ and calculates only one correction. Single-step algorithms solving only the linearized problem around a homogeneous starting model have been widely used (Isaacson *et al.* 1992; Lehmann 1995; Loke & Barker 1995; Perez-Flores & Gomez-Treviño 1997) and have proven to yield reasonable inversion results for low-contrast models.

The SVD inversion algorithm shown in Fig. 2 is used to determine the effective number of linear independent measurements

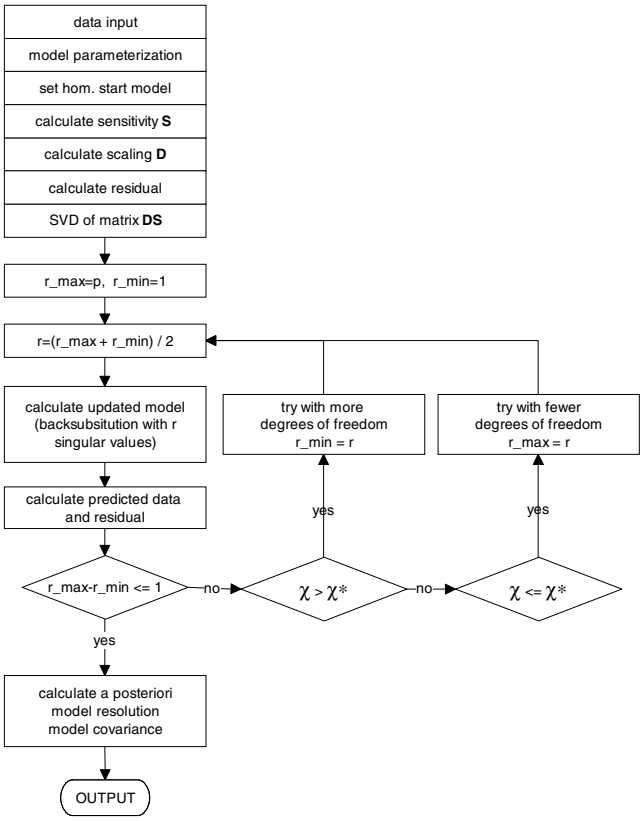

Figure 2. Flow chart of the SVD inversion program attaining a minimum structure model based on the least number of degrees of freedom needed to sufficiently fit the data.

and resolvable model eigenvectors r by means of a line search approach. Only such a number of model eigenvectors is incorporated in the solution as is necessary to fit the data to the prescribed target misfit.

After data input and a sufficiently fine model parametrization a homogeneous starting model is set, the sensitivity matrix is calculated analytically and scaled with the data variances. Next, the data residual vector is calculated and the system matrix decomposed. The first model estimate is calculated by a computationally inexpensive back-substitution after zeroing all singular values above index $p/2$. If the fit between the forward response of this model and the data is worse or better than the prescribed value the number of effective non-zero singular r values is increased or decreased, respectively. Repeating this procedure iteratively leads to a model of the least complexity of all models sufficiently fitting the data. Finally, model resolution and covariance are calculated on the basis of r degrees of freedom. As the algorithm internally uses logarithms of data and model parameters $\hat{d}_{i} = \ln d_{i}$ and $\hat{m}_{j} = \ln m_{j}$ and a homogeneous background, the general theory outlined in the previous section can be slightly refined by scaling as described in the appendix. Model resolution, data resolution and model covariance matrices are calculated by decomposition of the scaled matrices $\hat{\mathbf{D}}\hat{\mathbf{S}}$. Furthermore, it follows that each cell of the estimated model contains a geometrical weighted average of the true resistivity

$$m_{j}^{\text{est}} = \prod_{k=1}^{M} m_{k}{}^{R_{M,jk}}. \tag{24}$$

Finally, the diagonal elements of the logarithmic model covariance matrix can be scaled back to derive an estimate for the statistical

deviation δm_j^{est} of the non-logarithmic model resistivity relative to its expectation $\langle m_j^{\text{est}} \rangle$:

$$\frac{\delta m_j^{\text{est}}}{\langle m_j^{\text{est}} \rangle} = \left(e^{\delta \hat{m}_j^{\text{est}}} - 1 \right) \times 100 \,\text{per cent} \tag{25}$$

with

$$\delta \hat{m}_j^{\text{est}} = \sqrt{[\text{cov}\,\hat{\mathbf{m}}]_{jj}}.$$

It has to be noted that this measure does not reflect the relative standard deviation, because, owing to the non-linearity of the problem, the distribution of m_j^{est} is non-Gaussian.

4 NUMERICAL EXAMPLES

In this following example the generalized inverse algorithm is applied to synthetic data from a 2-D dc problem. First singular-value spectrum and model eigenvectors are inspected to obtain principal insight into non-uniqueness, then the model resolution is compared for accurate and inaccurate data, the results of inversion and image appraisal are presented and finally the data resolution matrix is discussed.

The experimental setup employed $L = 25$ electrodes arranged on a linear profile with a unit spacing of 1 m. The exemplary complete four-electrode data set comprised $L(L-3)/2 = 275$ theoretically linear independent measurements. It was based on a conventional dipole–dipole-γ set with a unit dipole width $a = 1$ and levels from $n = 1$ to 22. Since such a set comprises only $(L-2)(L-3)/2 = 253$ measurements and is therefore incomplete $L-3$ Schlumberger-like measurements were added employing a fixed current dipole at electrodes 1 and 25 and a moving unit dipole for voltage mapping. As the data set would form a symmetrical completion of a dipole–dipole set if electrodes were arranged in a circle, it is conventionally called a circulating dipole–dipole in medical impedance tomography. The data set was chosen because it performed very well in a comparison of eight different data sets (Friedel 2000) and furthermore the gain in information by additional non-conventional measurements becomes clear from the data resolution matrix.

The 2-D parameter domain consisted of a rectangle $x = [-2\,\text{m}, 26\,\text{m}], z = [0\,\text{m}, -10\,\text{m}]$ extending the electrode scheme horizontally by two unit spacings. The domain was parametrized into 1120 cells of 0.5×0.5 m^2 width and one additional parameter comprising the remaining outside background region. The latter was done to ensure $\int_\Omega S_i(m^{\text{hom}}, \mathbf{r}')\, d^3r = 1$ needed for the approximate forward procedure. The parametrization was chosen to be relatively fine to avoid inherent regularization of the inverse problem.

The parameter sensitivity matrix was calculated analytically for the homogeneous half-space using the Born approximation. In the strike direction a transformation in complete elliptic integrals was used (Lehmann 1995; Loke & Barker 1995). In the x–z plane Gauss–Legendre integration was used with an adaptive number of 36 to 9216 function evaluations per cell.

4.1 SVD spectrum and model eigenvectors

First insights into the information content of a forward map and the condition of the inverse can be gained by inspection of the spectrum of singular values. The SVD spectrum of the sensitivity matrix (Fig. 3) shows a nearly exponential decay illustrating the ill-posedness of the inverse problem. This result agrees well with findings from medical impedance tomography (Dobson & Santosa 1994).

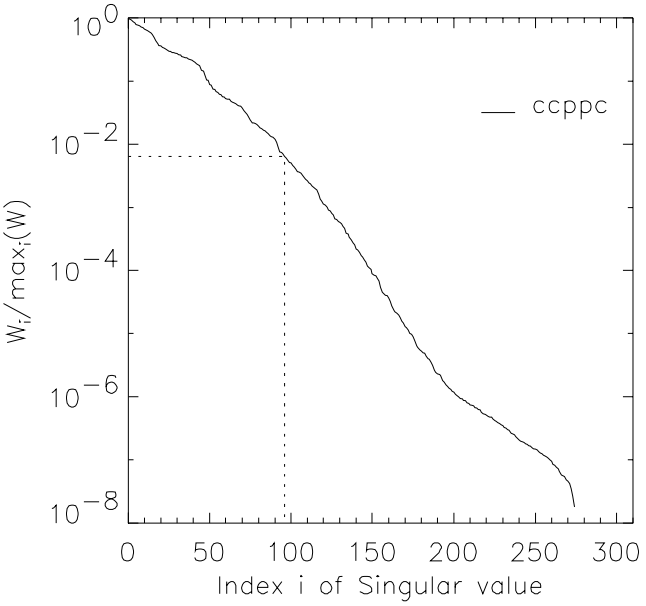

Figure 3. Normalized spectrum of the singular values for a circulating dipole–dipole data set. The exponential decay illustrates the ill-posedness of the inverse problem. The vertical line marks the number of degrees of freedom needed to fit the data in the example.

The decreasing spectrum of singular values corresponds to a succession of eigenvectors in the model domain sorted according to their distinguishability. This ordering makes the otherwise arbitrary choice of an orthonormal system in the space $\mathcal{M}$ unique. Fig. 4 shows selected model eigenvectors.

Typically we find symmetric and antisymmetric eigenvectors with respect to a vertical axis in the centre of the electrode array. High-frequency features often occur near the electrodes, but there is no unique relation between the index and the spatial wavelengths contained in the eigenvectors. However, high index eigenvectors usually show increased complexity, e.g. V_{275} which is effectively unresolvable with realistic noise. The remarkable symmetry of the eigenvectors may inspire new approaches to model parametrization. The conventional parametrization of models into large numbers of small blocks leads to huge sensitivity matrices and underdetermined systems, which have to be stabilized by subjective model constraints. Parametrization guided by model eigenvectors as natural degrees of freedom may be used in the future to reduce the dimension of the inverse problem without sacrificing unnecessarily resolution.

4.2 Resolving power of accurate and inaccurate data

If noise-free data are assumed, the generalized inverse need not be stabilized by truncation of the SV spectrum. All theoretically independent data are considered to be independent, the kernel of the forward map has the maximum rank $r = p$. Although impractical for real field data, calculation of the resolution matrix including all eigenvectors yields valuable insight into the maximum possible resolution of a measuring system. Fig. 5 illustrates model resolution for the given data set by depicting the point spread function for four typical cells. Cell 125 just 1 m below the electrode array is nearly perfectly resolvable. The same applies to cell 588 at medium depths beneath the horizontal centre of the electrode spread. The averaging kernel for cell 348 at lesser depth but off the centre is much wider, indicating a poorer resolution in this region. Cell 722 located at a

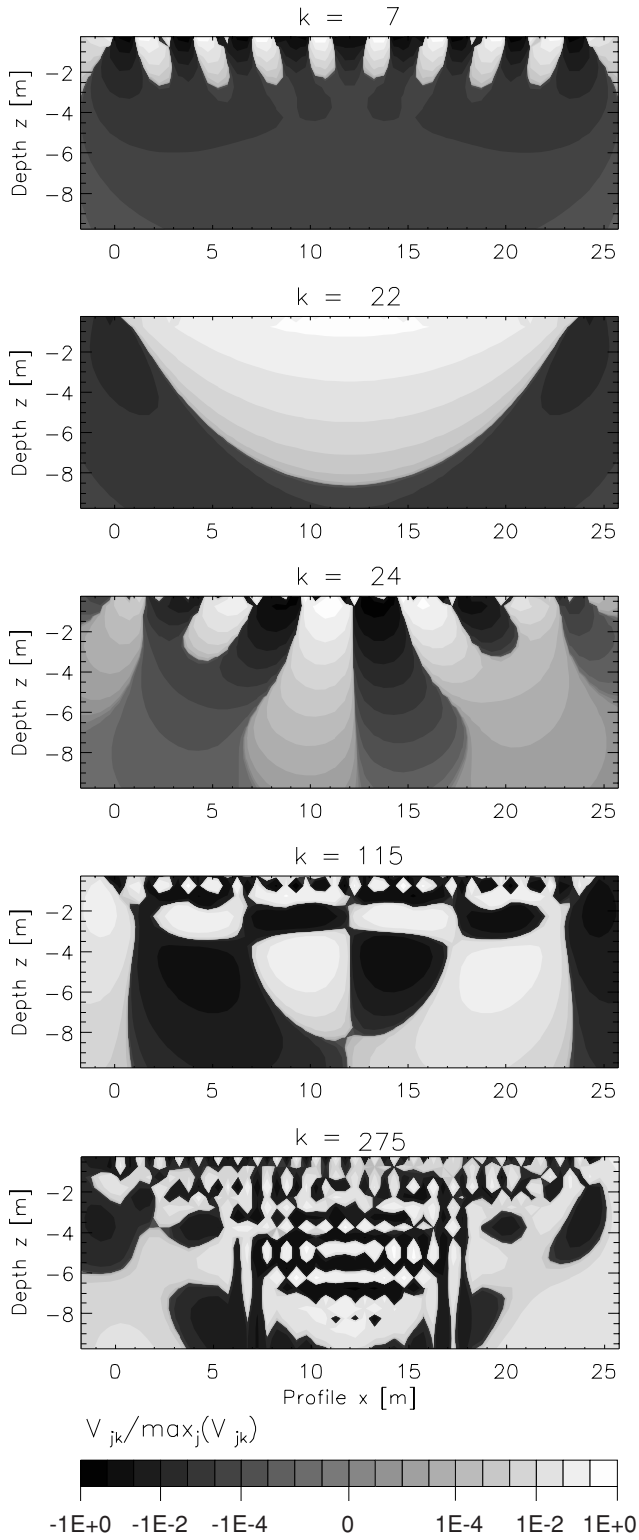

Figure 4. Selected eigenvectors of the sensitivity matrix in the model domain. For vector 275 which is practically unresolvable, the otherwise occurring symmetry or antisymmetry is broken owing to numerical effects.

depth of 6 m and horizontally near the end of the electrode system lies in a region of very poor image quality. The averaging kernel is inflated to enormous size, its maximum is not located on the diagonal element and has significant negative side lobes. In this area the image will not only be of poor contrast but also geometrically distorted.

Although browsing through the point spread function of individual cells is very instructive, it is laborious and the information content of $\mathbf{R}_M$ needs to be condensed to more practical measures. For this purpose the diagonal elements of $\mathbf{R}_D$ or the deviation of $\mathbf{R}_D$ from the identity (Menke 1989) are often considered. When talking to experimentalists and users a scaling of the diagonal elements into a readily understandable measure seems favourable. A value of 1 in a diagonal element means that the average of the respective parameter cell can be resolved uniquely. Assuming a boxcar-like resolving kernel with an amplitude of 0.25 located around the diagonal element would mean that the average of four cells can be resolved uniquely. This motivates the definition of a *radius of resolution*

$$r_{\mathrm{res},j} = \frac{r_0}{\sqrt{R_{M,jj}}} \tag{26}$$

for each region centred around the mid-point of parameter cell j. Here πr_0^2 equals the area of the uniform parameter cell. This obviously simplest way to scale diagonal elements may serve as a first measure of resolution and can be replaced by the computationally more demanding estimate of the half-width of the point spread function. Since both are inadequate for cells with asymmetrical or otherwise deformed weighting kernels, at least an additional indication of geometrical distortion is needed, which most primitively can be introduced as a *distortion flag*,

$$f_i = \mathrm{not}\left(\mathbf{R}_{M,ii} = \max_k \mathbf{R}_{M,ik}\right)$$

which indicates that the maximum of the point spread function is off-diagonal. The bottom diagram of Fig. 5 summarizes the information contained in the diagonal elements: the colourscale corresponds to the value of the diagonal element scaled in terms of a radius of resolution and a white square indicates a distortion flag of zero.

Both measures independently mark out a triangular area of high image quality below the electrode system, where high resolution and no or little distortion can be expected. The edges of the triangle form an angle of approximately 38° to the surface.

If a realistic data error is accounted for, the approximate inverse procedure inevitably needs to be stabilized, which is achieved here by using only the first r eigenvectors and singular values for the construction of the inverse and the appraisal functionals. Fig. 6 illustrates selected resolving kernels for a truncated inverse with only 96 degrees of freedom resulting from realistic noise specified in the next section. Near the surface, resolution is still good, but at greater depth, the resolving kernels are much wider and show geometrical distortion. As an extreme example, image cell 722 contains an average of resistivities in a completely different area and therefore lies well beyond the depth of investigation. The formerly triangular area of good resolution and little distortion derived from the diagonal element collapses to a bathtub-like area.

It is worth noting that the quality functionals are calculated for a specific model parametrization, which implicitly regularizes the problem. However, if a sufficiently fine parametrization were chosen the radius of resolution and distortion flag prove to be very consistent, suggesting that they can be motivated by a continuous theory, as pointed out by Dobson & Santosa (1994) for the unit disc model domain.

4.3 Inversion result and image quality

After introducing model resolution for full and truncated SVD inverse, the inversion result itself will now be discussed. The model

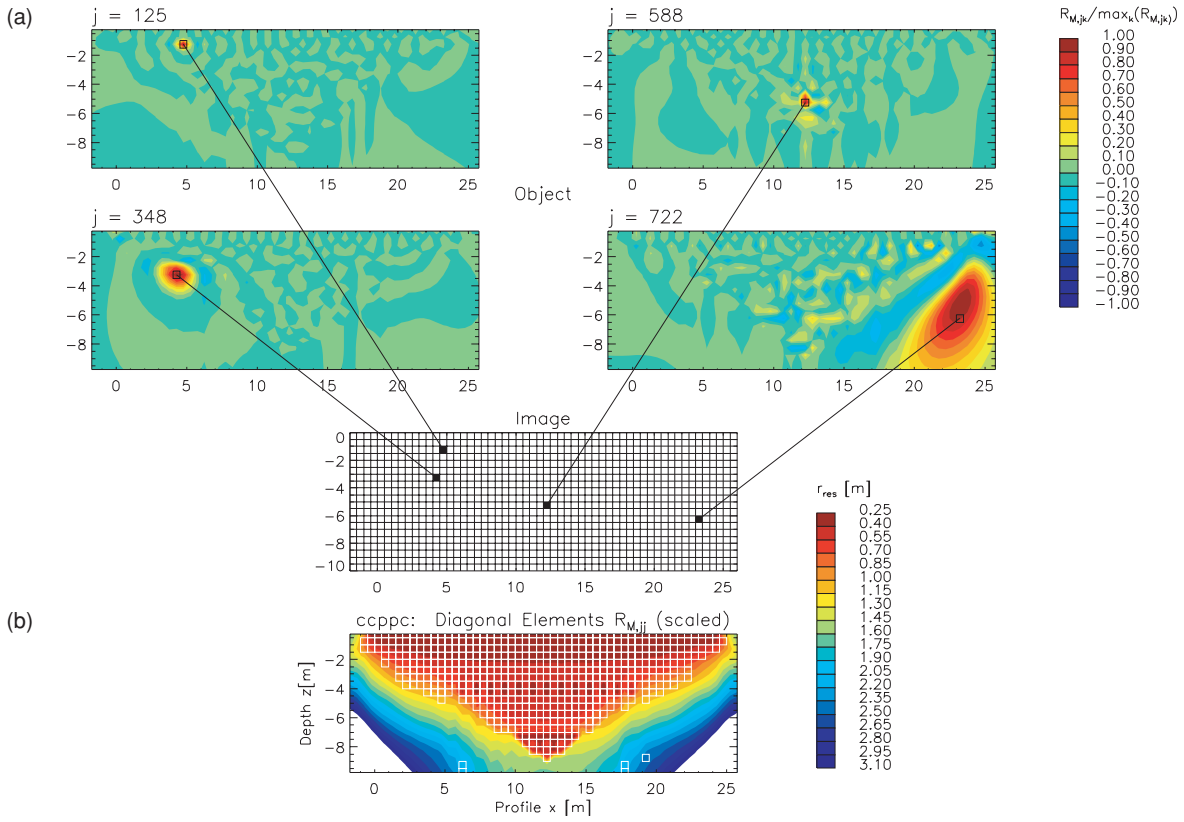

Figure 5. Top, resolving kernels for four selected cells assuming accurate data considering all 275 model eigenvectors. Bottom, colour represents the radius of resolution as derived from the diagonal elements of the resolution matrix, white squares mark cells with zero distortion flag.

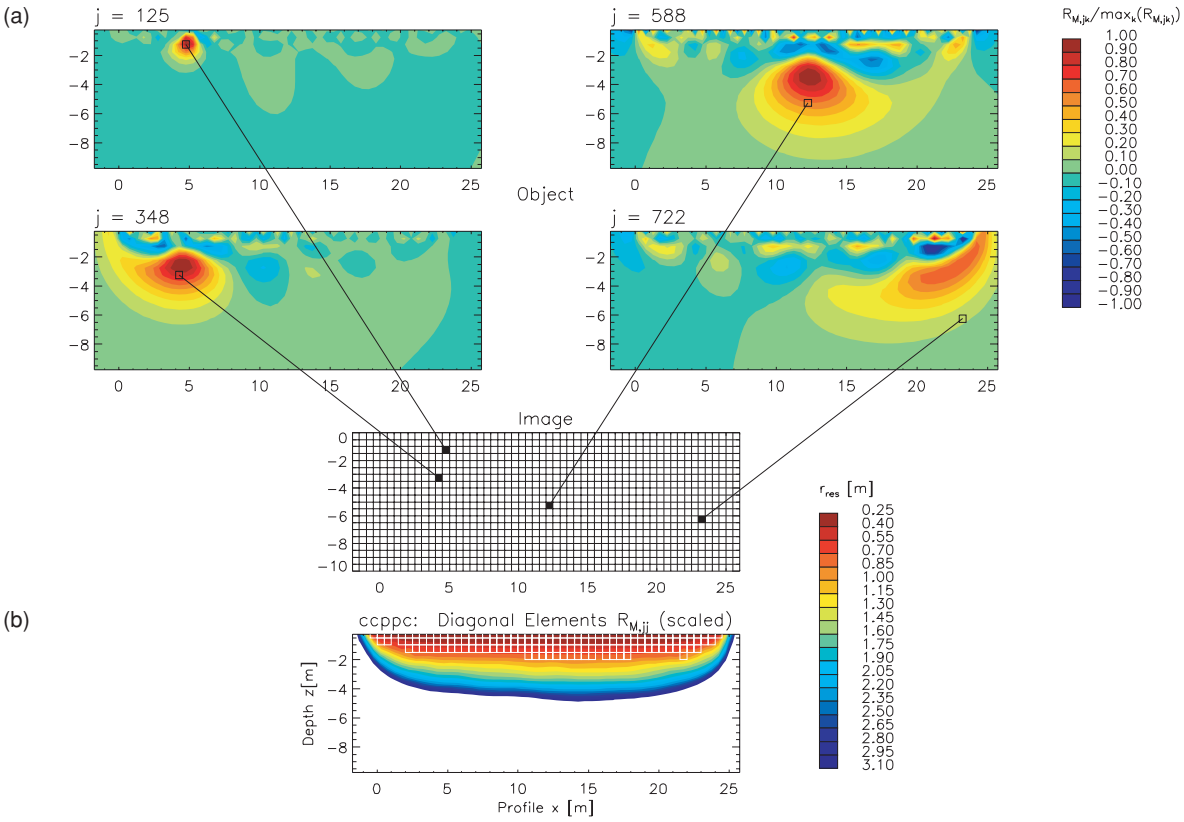

Figure 6. Top, resolving kernels for four selected cells assuming realistic data error considering only 96 of 275 model eigenvectors. Bottom, colour represents the radius of resolution as derived from the diagonal elements of the resolution matrix, white squares mark cells with zero distortion flag.

shown in Fig. 7(a) consisted of two rectangular blocks of 10 and 1000 Ωm embedded in a homogeneous half-space of 100 Ωm. Data were calculated synthetically using an FD forward algorithm. All data were contaminated with Gaussian noise but not with uniform variance. Experience from many field data sets shows that for configurations with a high geometrical factor (e.g. a dipole–dipole with large separations), the main contribution to the total error arises from inaccuracy in voltage measurements. The standard deviation is usually higher the closer the voltage comes to a site and instrument dependent minimum voltage $U_{\min}$ at which readings are mainly statistical. To account for such behaviour in a synthetic data set, the standard deviation of each measurement was estimated as follows:

$$\frac{\sigma_i}{d_i} = 1\,\text{per cent} + \frac{U_{\min}}{U_i} \times 100\,\text{per cent}.$$

For the given example of a near-surface ERT data set a driving current of 100 mA and a minimum voltage of 50 μV were assumed. The corresponding standard deviations varied between 1 per cent for configurations with the largest and 20 per cent for those with the smallest measured voltages.

The inversion scheme presented in Fig. 2 required a 96 degrees of freedom to fit the data to a target misfit of 1 corresponding to an rms error of 4 per cent. The inverted image (Fig. 7b) shows that the low-resistivity body was well reconstructed in location and amplitude (9 Ωm), whereas for the high-resistivity body only the upper edge could be resolved and its contrast is clearly to small. This can be explained with a resolution matrix (Fig. 7c). At a depth of 4 m its radius of resolution is approximately 3 m, indicating that the image in that region contains averages of a volume much larger than the body itself. Image noise is seen in the model and the corresponding model covariance matrix (Fig. 7d) predominantly at shallow depths beneath the electrodes, where resolution is high. Noise is not projected into the unresolvable regions at greater depths where it is usually encountered for smoothness-constrained inversion algorithms (Alumbaugh & Newman 2000). The magnitude of the image noise estimated by the covariance matrix seems slightly too small in comparison with that estimated from the image itself.

4.4 Efficiency of the data set

The relative importance of an individual data point in the set of configurations can be estimated from the data resolution matrix. For accurate data all measurements are linearly independent and $\mathbf{R}_D$ equals unity. For inaccurate data only weighted averages of the measured data can be predicted. Fig. 8 illustrates data resolution for the noisy data set and 96 incorporated degrees of freedom. The dipole–dipole measurement 86 in level 2 carries nearly unique information, for deeper levels data become increasingly correlated, mostly upward in the pseudosection, indicating that wide spacing measurements contain much information that is already contained in a set of shallower measurements. Furthermore, correlations occur predominantly along diagonals of the pseudosection, i.e. for measurements with coincident voltage or current dipole positions (measurement 179). As for the model resolution matrix, information can be condensed by depicting only the diagonal elements of $\mathbf{R}_D$. Clearly, data importance decreases with higher levels. This analysis justifies theoretically the often empirically motivated practice of alternatively sparsing out measurements or increasing the dipole width at high levels. Most noteworthy is the importance of the additional Schlumberger-like measurements, depicted as an extra row on top of each triangular pseudosection. In particular, the most asymmetrical of these configurations possess a higher information content than many of the classical dipole–dipole configurations. If multi-electrode field equipment allows, the measurement of such configurations is recommended. A more detailed comparison of data sets is presented in Friedel (2000).

5 DISCUSSION AND CONCLUSIONS

In this paper, a single-step linearized inversion scheme for dc resistivity data was presented that uses a truncated SVD inverse. Controlled smoothness and minimum complexity of the solution is achieved by a line search approach to determine the truncation value, i.e. the maximum number of degrees of freedom necessary to fit the data to a prescribed target misfit.

As SVD is well known to be a computationally expensive and slow procedure the method may never compete with faster algorithms. Its great virtue, however, is that it avoids empirically defined smoothness constraints that might be inappropriate to the resolving power of the experimental design. Insight from SVD analysis may, in contrast, be used as a guideline for the design of optimized experimental setup, choice of parametrization and model smoothness functionals. A comparison of various data sets will be the subject of a subsequent paper.

Besides a resistivity image, the algorithm produces estimates of model resolution, model covariance and data resolution. For a low-contrast approximation these estimates can be given *a priori*. If the algorithm is incorporated in a full non-linear inversion scheme and the sensitivity matrix for the final model estimate is used *a posteriori* estimates can be derived. The crucial assumption here is that the model found is linearly close to the true model.

However, analysis of the resolving power in a numerical example suggests that the non-uniqueness in the electrical resistivity tomography problem arises possibly to a greater degree from its ill-posedness than from non-linearity.

In a numerical example the linearized single-step scheme provided reasonable agreement between the image and the input model, although the latter contained moderate resistivity contrasts of 10:100:1000 Ωm. On the other hand, the resolving power of an exemplary complete four-electrode data set containing classical dipole–dipole and non-conventional configurations is severely affected by data inaccuracy. Even for perfect data a clearly defined area could be marked out to which an image of high resolution and free of geometrical distortion is restricted. For noisy data, this area shrinks drastically as the weighting kernel functions for given cells are inflated and groups of parameters and predicted data become increasingly correlated. In the example, the ill-posedness of the inverse problem can be quantified by the number of effectively resolvable degrees of freedom in the image (96) which was only 35 per cent of the number of data (275) and less than 9 per cent of the size of the parameter space (1121). These numbers underline the need for optimized approaches to the design of experiments and inversion schemes. Although the theory presented in this paper is only linear, quantification of the quality of resistivity tomograms and the efficiency of the imaging process may be used as a guideline in this way.

To comply with the field users need for few representative and readily understandable quality estimates for the image, three space-dependent scalar quantities were introduced: a radius of resolution, a distortion flag and a percentage of image noise. The radius of resolution is calculated from the diagonal elements of the model covariance matrix assuming that the resolving kernel is localized and nearly a boxcar. Deviations from this assumption are mapped into the second quantity, the distortion flag, which indicates possible

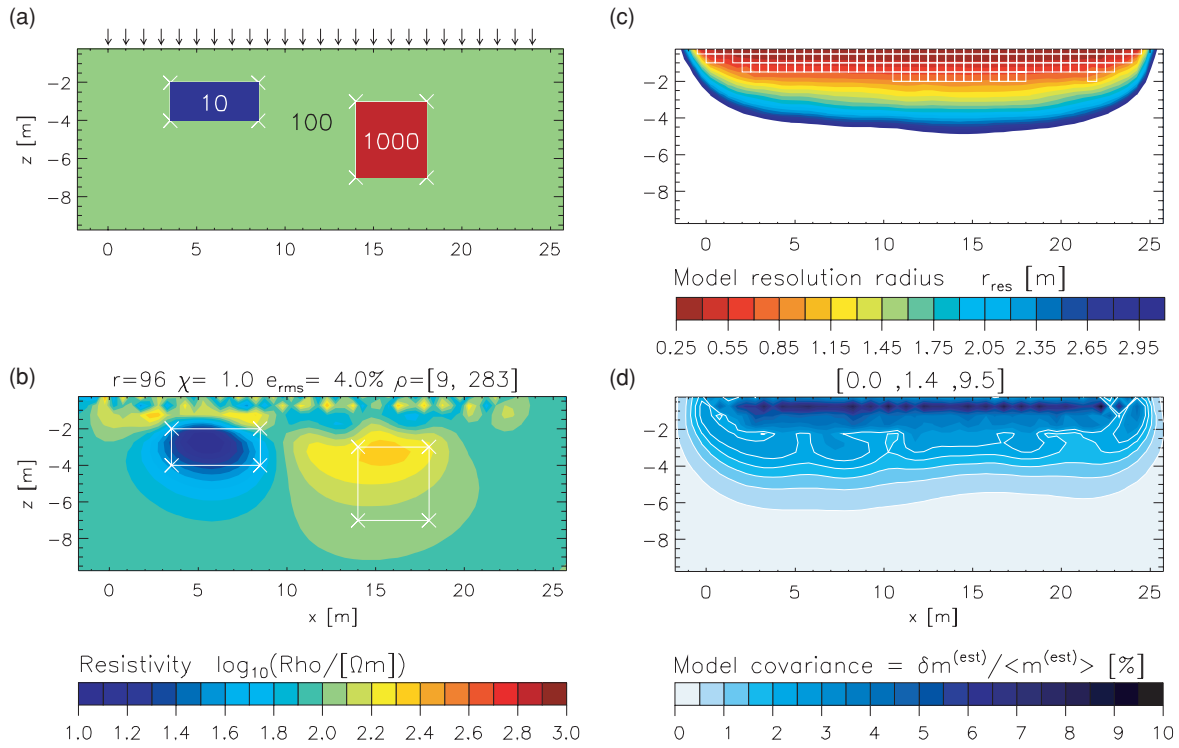

Figure 7. (a) Synthetic input model with two bodies embedded in a homogeneous half-space, (b) inversion result, (c) diagonal elements of resolution matrix scaled to radius of resolution and (d) model covariance matrix scaled to the percentage of image noise of apparent resistivity.

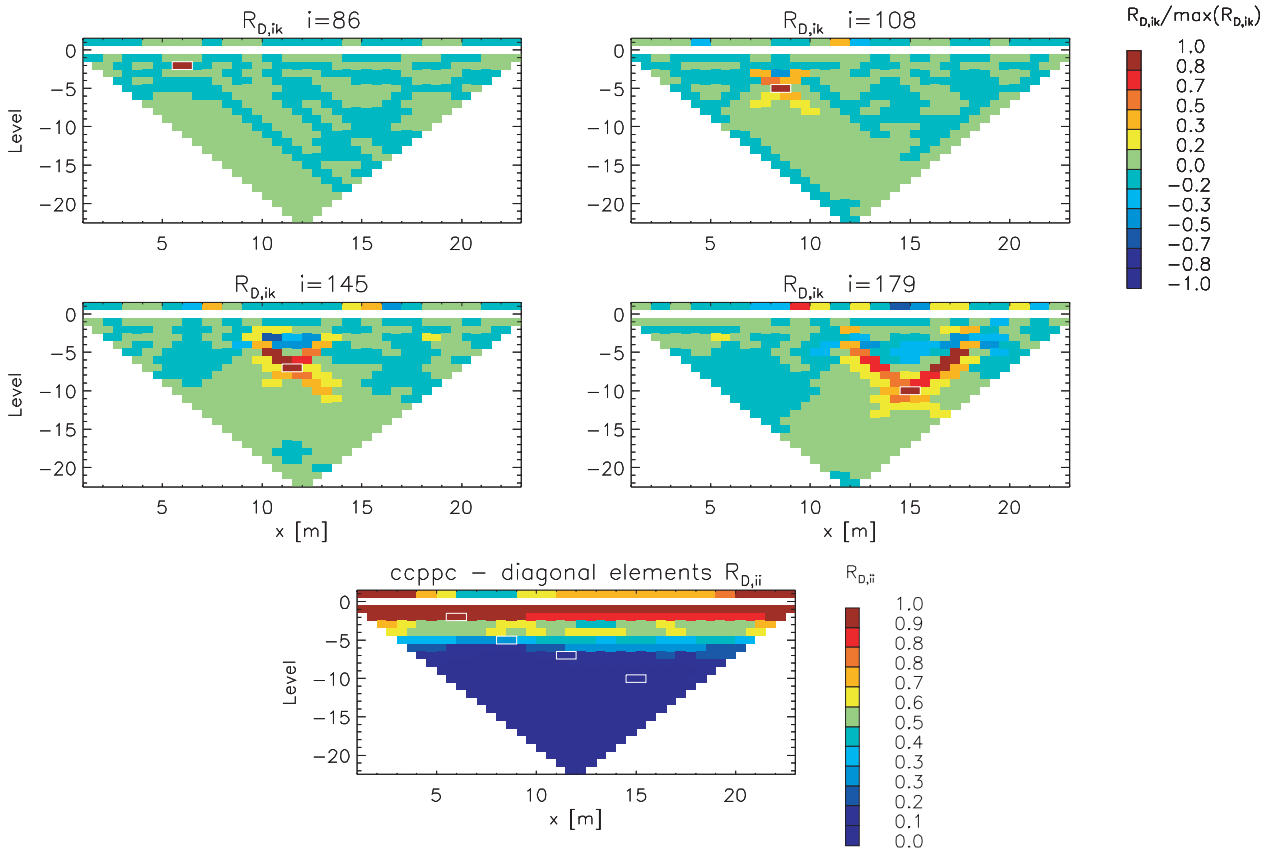

Figure 8. Data resolution matrix assuming realistic noise. Top: averaging kernels for four selected datum points. Bottom: diagonal elements of the model resolution matrix. In each diagram the importance of dipole–dipole data is presented in form of a pseudo-section, whereas values for additional asymmetric Schlumberger-like measurements are depicted in an extra row on top.

geometrical distortions in the image. Though both measures were calculated for a certain model parametrization, numerical experiments with finer discretizations proved to be consistent.

The deduction of the simplified functionals from the model resolution and covariance matrices is an attempt to condense the enormous amount of information contained in the model resolution and covariance matrix to user-friendly quantities. As such they are first and evidently crude approximations and subject to refinement as theory advances.

ACKNOWLEDGMENTS

I wish to thank Prof. Franz Jacobs and Dr Hansruedi Maurer for fruitful discussions and Prof. Ulrich Achauer and an anonymous reviewer for their helpful comments on the manuscript. I also wish to thank Jeremy Heighway for reviewing the English. This work was partially supported by the Deutsche Forschungsgemeinschaft Ja 590/6.

REFERENCES

Aki, K. & Richards, P.G., 1980. *Quantitative Seismology,* Freeman, San Francisco, CA.

Alumbaugh, D.L. & Newman, G.A., 2000. Image appraisal for 2-D and 3-D electromagnetic inversion, *Geophysics,* **65,** 1455–1467.

Apparao, A., Rao, T.G., Sastry, R.S. & Sarma, V.S., 1992. Depth of detection of buried conductive targets with different electrode arrays in resistivity prospecting, *Geophys. Prospect.,* **40,** 749–760.

Avis, N. & Barber, D.C., 1994. Image reconstruction using non-adjacent drive currents, *Clin. Phys. Physiol. Meas.,* **15,** 153–160, Suppl. A.

Backus, G. & Gilbert, F., 1968. The resolving power of gross earth data, *Geophys. J. R. astr. Soc.,* **16,** 169–205.

Barker, R.D., 1979. Signal contribution sections and their use in resistivity studies, *Geophys. J. R. astr. Soc.,* **59,** 123–129.

Barker, R.D., 1989. Depth of investigation of colinear symmetrical four electrode arrays, *Geophysics,* **54,** 1031–1037.

Beard, L.P. & Tripp, A.C., 1995. Investigating the resolution of IP arrays using inverse theory, *Geophysics,* **60,** 1326–1341.

Beard, L.B., Hohmann, G.W. & Tripp, A.C., 1996. Fast resistivity/IP inversion using a low contrast approximation, *Geophysics,* **61,** 169–179.

Brunner, I., Friedel, S., Jacobs, F. & Danckwardt, E., 1999. Investigation of a tertiary maar structure using 3-D resistivity imaging, *Geophys. J. Int.,* **136,** 771–780.

Dahlin, T. & Bing, Z., 2001. A numerical comparison of 2D resistivity imaging with eight electrode arrays, in *Procs. EEGS'01*, *Birmingham*, EEGS.

Dahlin, T. & Loke, M.H., 1998. Resolution of 2D-Wenner resistivity imaging as assessed by numerical modelling, *J. Appl. Geophys.,* **38,** 237–249.

deGroot-Hedlin, C. & Constable, S.C., 1990. Occam's inversion to generate smooth, two-dimensional models from magnetotelluric data, *Geophysics,* **55,** 1613–1624.

Dey, A., Meyer, W.H., Morrison, H.F. & Dolan, W.M., 1975. Electric field response of two dimensional inhomogeneities to unipolar and bipolar electrode configurations, *Geophysics,* **40,** 630–640.

Dobson, D.C. & Santosa, F., 1994. Resolution and stability analysis of an inverse problem in electrical impedance tomography: dependence on input current patterns, *SIAM J. Appl. Math.,* **54,** 1342–1360.

Evjen, H.M., 1938. Depth factors and resolving power of electrical measurements, *Geophysics,* **3,** 78–95.

Friedel, S., 1997. Inversion in der Geoelektrik auf der Grundlage sensitiver Bereiche und algebraischer Rekonstruktionstechniken, *Leipziger Geowissenschaften,* **3,** 33–39.

Friedel, S., 2000. Über die Abbildungseigenschaften der geoelektrischen Impedanztomographie unter Berücksichtigung von endlicher Anzahl und endlicher Genauigkeit der Meßdaten, Berichte aus der Geowissenschaft, Shaker, Aachen, *Dissertation,* Universität Leipzig.

Golub, G.H. & van Loan, C.F., 1989. *Matrix Computations,* 2nd edn, John Hopkins University Press, New York.

Gómez-Treviño, E., 1987. Nonlinear integral equations for electromagnetic inverse problems, *Geophysics,* **52,** 1297–1302.

Inman, J.R., Ryu, J. & Ward, S.H., 1973. Resistivity inversion, *Geophysics,* **38,** 1088–1108.

Isaacson, D., Cheney, M. & Newell, J.C., 1992. Problems in impedance imaging, in *Inverse Problems in Mathematical Physics,* pp. 62–70, eds Päivärinta, L. & Somersalo, E., Springer, Saariselkä.

Iyer, H.M. & Hirahara, K., eds., 1993. *Seismic Tomography: Theory and Practice,* Chapman and Hall, London.

Kemna, A., 1995. Tomographische Inversion des spezifischen Widerstandes in der Geoelektrik, *Diplomarbeit,* Universität Köln.

Kohn, R. & Vogelius, M., 1985. Determining the conductivity by boundary measurements II, interior results, *Comm. Pure Appl. Math.,* **38,** 644–667.

LaBrecque, D., Miletto, M., Daily, W., Ramirez, A. & Owen, E., 1996. The effects of noise on Occam's inversion of resistivity tomography data, *Geophysics,* **61,** 538–548.

Langer, R.E., 1933. An inverse problem in differential equations, *Am. Math. Soc. Bull.,* **29,** 814–820.

Lehmann, H., 1995. Potential representation by independent configurations on a multi-electrode grid, *Geophys. J. Int.,* **120,** 331–338.

Loke, M.H. & Barker, R.D., 1995. Least-squares deconvolution of apparent resistivity pseudosections, *Geophysics,* **60,** 1682–1690.

Maurer, H. & Boerner, D.E., 1998. Optimized and robust experimetal design: a non-linear application to EM sounding, *Geophys. J. Int.,* **132,** 458–468.

Maurer, H., Boerner, D.E. & Curtis, A., 2000. Design strategies for electromagnetic geophysical surveys, *Inverse Problems,* **16,** 1097–1117.

Menke, W., 1989. *Geophysical Data Analysis: Discrete Inverse Theory,* International Geophysics Series, Vol. 45, Academic Press, London.

Minkoff, S.E., 1996. A computationally feasible approximate resolution matrix for seismic inverse problems, *Geophys. J. Int.,* **126,** 345–359.

Nolet, G., ed., 1987. *Seismic Tomography,* Reidel, Hingham, MA.

Olayinka, A.I. & Weller, A., 1997. The inversion of geoelectrical data for hydrogeological applications in crystalline basement areas of Nigeria, *J. Appl. Geophys.,* **37,** 85–102.

Olayinka, A.I. & Yaramanci, U., 2000. Assessment of the reliability of 2d inversion of apparent resistivity data, *Geophys. Prospect.,* **48,** 293–316.

Oldenburg, D.W., 1978. The interpretation of direct current resistivity measurements, *Geophysics,* **43,** 610–625.

Oldenburg, D.W., 1983. Funnel functions in linear and nonlinear appraisal, *J. geophys. Res.,* **88,** 7387–7398.

Oldenburg, D.W. & Li, Y., 1999. Estimating the depth of investigation in dc resistivity and IP surveys, *Geophysics,* **64,** 403–416.

Park, S.K. & Van, G.P., 1991. Inversion of pole–pole data for 3-d resistivity structure beneath arrays of electrodes, *Geophysics,* **56,** 951–960.

Perez-Flores, M.A. & Gomez-Treviño, E., 1997. Dipole–dipole resitivity imaging of the Ahuachapan-Chipilapa geothermal field, El Salvador, *Geothermics,* **26,** 657–680.

Sasaki, Y., 1992. Resolution of resistivity tomography inferred from numerical simulation, *Geophys. Prospect.,* **40,** 453–463.

Seichter, M., 1998. Rekonstruktion der räumlichen Verteilungen komplexer elektrischer Leitfähigkeiten, *Dissertation,* Universität Braunschweig.

Shim, Y.S. & Cho, Z.H., 1981. SVD pseudo-inversion image reconstruction, *IEEE Trans. Acous. Speech, Signal Processing,* **ASSP-32**, 904–909.

Spitzer, K., 1998. The three-dimensional dc sensitivity for surface and subsurface sources, *Geophys. J. Int.,* **134,** 736–764.

Sylvester, J. & Uhlmann, G., 1987. A global uniqueness theorem for an inverse boundary value problem, *Ann. Math.,* **125,** 153–169.

van Nostrand, R.G., 1953. Limitations on resistivity methods as inferred from the buried sphere problem, *Geophysics,* **18,** 423–433.

APPENDIX A: SPECIFICA OF THE LOG PROBLEM

Because rock resistivity varies over many orders of magnitude, electromagnetic methods often use logarithms of resistivity $\hat{m}_j = \ln m_j$ as parameters and logarithms of apparent resistivity as data $\hat{d}_i = \ln d_i$ (Park & Van 1991; Beard *et al.* 1996; Olayinka & Weller 1997). This appendix describes the consequences of such logarithmic scaling on the estimates of resolution, stability and efficiency.

The logarithmic problem can be linearized as follows:

$$\hat{d}_i = \hat{d}_i^0 + \sum_{j=1}^{M} \left.\frac{\partial \hat{d}_i}{\partial \hat{m}_j}\right|_{m=m^0} \left(\hat{m}_j - \hat{m}_j^0\right) \tag{A1}$$

with

$$\frac{\partial \hat{d}_i}{\partial \hat{m}_j} = \frac{\partial \ln d_i}{\partial \ln m_j} = \frac{\partial \ln d_i}{\partial d_i}\frac{\partial d_i}{\partial m_j}\frac{\partial m_j}{\partial \ln m_j} = \frac{m_j^0}{d_i^0} S_{ij}. \tag{A2}$$

For a homogeneous starting model resistivity and apparent resistivity are equal $d_i^0 = m_j^0$ and obtain $\hat{\mathbf{S}} = \mathbf{S}$ and

$$\Delta\hat{\mathbf{d}} = \mathbf{S}\Delta\hat{\mathbf{m}}. \tag{A3}$$

When using logarithmic data and parameters in the quasi-homogeneous case the sensitivity matrix need not be scaled. Furthermore, it follows from $\sum_{j=1}^{M} S_{\mathrm{ij}} = 1$ that

$$\hat{d}_i = \sum_{j=1}^{M} S_{\mathrm{ij}} \hat{m}_j, \tag{A4}$$

which allows a linearized forward algorithm for the quasi-homogeneous case.

The logarithmic transformation requires scaling of the data covariance matrix. If a datum d_i is characterized by its expectation $\langle d_i \rangle$ and a statistical disturbance δd_i

$$d_i = \langle d_i \rangle + \delta d_i = \langle d_i \rangle \left(1 + \frac{\delta d_i}{\langle d_i \rangle}\right), \tag{A5}$$

then it follows for the logarithm

$$\hat{d}_i = \ln d_i = \ln\langle d_i \rangle + \ln\left(1 + \frac{\delta d_i}{\langle d_i \rangle}\right) = \langle \hat{d}_i \rangle + \delta\hat{d}_i. \tag{A6}$$

The diagonal elements of the new scaling matrix $\hat{\mathbf{D}}$ should characterize the reciprocal deviation of the logarithmic data. Although the logarithmic data may not strictly follow a Gaussian distribution it seems reasonable to approximate the data covariance matrix elements by $\hat{D}_{ii} = 1/\ln(1 + \sigma_i/d_i)$.

By minimizing the functional

$$\|\hat{\mathbf{D}}(\Delta\hat{\mathbf{d}} - \hat{\mathbf{S}}\hat{\Delta}\hat{\mathbf{m}})\| = \min! \tag{A7}$$

using the generalized inverse one obtains for accurate data in analogy to eq. (19) the relation

$$\hat{m}_j^{\mathrm{est}} = \hat{m}_j^0 + \sum_{k=1}^{M} R_{M,jk}\left(\hat{m}_k - \hat{m}_k^0\right) \tag{A8}$$

for the logarithmic parameters where the resolution matrix is given by $\mathbf{R}_M = (\hat{\mathbf{D}}\hat{\mathbf{S}})^{\dagger}(\hat{\mathbf{D}}\hat{\mathbf{S}})$. For the resistivities it follows that

$$m_j^{\mathrm{est}} = m_j^0 \prod_{k=1}^{M} \left(\frac{m_k}{m_k^0}\right)^{R_{M,jk}}. \tag{A9}$$

Because $\sum_{j=1}^{M} R_{M,jk} = 1\,\forall k$ and a homogeneous starting model $\mathbf{m}^0$ is assumed it follows furthermore that

$$m_j^{\mathrm{est}} = \prod_{k=1}^{M} {m_k}^{R_{M,jk}}. \tag{A10}$$

The model estimate obviously contains the geometrically weighted average of the object resistivities. An analogous relation can be derived for the data resolution matrix $\mathbf{R}_D = (\tilde{\mathbf{D}}\hat{\mathbf{S}})(\hat{\mathbf{D}}\hat{\mathbf{S}})^{\dagger}$.

The matrix $[\mathrm{cov}\,\hat{\mathbf{m}}^{\mathrm{est}}] = (\hat{\mathbf{D}}\hat{\mathbf{S}})^{\dagger}[\mathrm{cov}\,\hat{\mathbf{d}}](\hat{\mathbf{D}}\hat{\mathbf{S}})^{\dagger\mathrm{T}}$ yields an estimate for the statistical deviation of the logarithmic parameters. For practical purposes it might be desirable to scale this back into a statistical error of resistivity.

If the logarithmic parameter is given by its expectation and a statistical disturbance

$$\hat{m}_j^{\mathrm{est}} = \langle \hat{m}_j^{\mathrm{est}} \rangle + \delta\hat{m}_j^{\mathrm{est}}. \tag{A11}$$

it follows for the resistivity that

$$m_j^{\mathrm{est}} = \langle m_j^{\mathrm{est}} \rangle \mathrm{e}^{\delta\hat{m}_j^{\mathrm{est}}} = \langle m_j^{\mathrm{est}} \rangle + \langle m_j^{\mathrm{est}} \rangle \left(\mathrm{e}^{\delta\hat{m}_j^{\mathrm{est}}} - 1\right) \tag{A12}$$

$$= \langle m_j^{\mathrm{est}} \rangle + \delta m_j^{\mathrm{est}} \tag{A13}$$

and the percentage of resistivity image noise becomes

$$\frac{\delta m_j^{\mathrm{est}}}{\langle m_j^{\mathrm{est}} \rangle} = (\mathrm{e}^{\delta\hat{m}_j^{\mathrm{est}}} - 1) \times 100\,\mathrm{per\,cent}, \tag{A14}$$

where the statistical deviation of the logarithmic parameter may be approximated by the diagonal element of the model covariance matrix $\delta\hat{m}_j^{\mathrm{est}} = \sqrt{[\mathrm{cov}\,\hat{\mathbf{m}}]_{jj}}$. When using such a scaled measure convenient for intuitive appraisal of a resistivity image, it has to be noted that it is a simplification and does not represent the percentage of standard deviation since, owing to the non-linearity of the problem, the errors in $\hat{\mathbf{d}}$, $\hat{\mathbf{m}}$ and $\hat{\mathbf{m}}^{\mathrm{est}}$ may not follow Gaussian statistics.